Localized artificial viscosity stabilization of discontinuous Galerkin methods for nonhydrostatic mesoscale atmospheric modeling

Meilin Yu [a], Francis X. Giraldo [b], Melinda Peng [c], and Z.J. Wang [a]

[a] The University of Kansas, Lawrence, KS 66045, USA
[b] Naval Postgraduate School, Monterey, CA 93943, USA
[c] U.S. Naval Research Laboratory, Monterey, CA 93943, USA

Abstract

Gibbs oscillation can show up near flow regions with strong temperature gradients in the numerical simulation of nonhydrostatic (NH) mesoscale atmospheric flows when using the high-order discontinuous Galerkin (DG) method. We propose to incorporate localized Laplacian artificial viscosity in the DG framework to suppress the spurious oscillation in the vicinity of sharp thermal fronts, while not contaminating the smooth flow features elsewhere. The resulting numerical formulation is then validated on several benchmark test cases, including a shock discontinuity problem with the 1D Burger's equation, and two test cases for the compressible Euler equations: a rising thermal bubble and density current. The results indicate that the proposed DG-localized Laplacian artificial viscosity method works robustly with a wide range of grid sizes and polynomial orders.

1. Introduction

Numerical weather prediction (NWP) models have been profoundly influenced by the paradigm shift in high performance computing (HPC). On the one hand, the ever increasing computing power allows researchers to run nonhydrostatic (NH) models at resolutions finer than 10 km [1]; on the other, both HPC and the intrinsic complex physical processes in NH modeling pose many challenges to the development of numerical methods, e.g., local numerical algorithms, high-order accuracy, geometric flexibility, etc. The discontinuous Galerkin (DG) method has been proven to be an ideal candidate to accommodate these challenges [2]. One example is the Nonhydrostatic Unified Model of the Atmosphere (NUMA) [3, 4], which has been successfully

1

Report Documentation Page

1. REPORT DATE **2014**	2. REPORT TYPE	3. DATES COVERED **00-00-2014 to 00-00-2014**

4. TITLE AND SUBTITLE	5a. CONTRACT NUMBER
Localized artificial viscosity stabilization of discontinuous Galerkin methods for nonhydrostatic mesoscale atmospheric modeling	5b. GRANT NUMBER
	5c. PROGRAM ELEMENT NUMBER
6. AUTHOR(S)	5d. PROJECT NUMBER
	5e. TASK NUMBER
	5f. WORK UNIT NUMBER

7. PERFORMING ORGANIZATION NAME(S) AND ADDRESS(ES) **Naval Postgraduate School,Monterey,CA,93943**	8. PERFORMING ORGANIZATION REPORT NUMBER

9. SPONSORING/MONITORING AGENCY NAME(S) AND ADDRESS(ES)	10. SPONSOR/MONITOR'S ACRONYM(S)
	11. SPONSOR/MONITOR'S REPORT NUMBER(S)

12. DISTRIBUTION/AVAILABILITY STATEMENT
Approved for public release; distribution unlimited

13. SUPPLEMENTARY NOTES
Journal of Computational Physics (in review 2014)

14. ABSTRACT
Gibbs oscillation can show up near flow regions with strong temperature gradients in the numerical simulation of nonhydrostatic (NH) mesoscale atmospheric flows when using the highorder discontinuous Galerkin (DG) method. We propose to incorporate localized Laplacian artificial viscosity in the DG framework to suppress the spurious oscillation in the vicinity of sharp thermal fronts, while not contaminating the smooth flow features elsewhere. The resulting numerical formulation is then validated on several benchmark test cases, including a shock discontinuity problem with the 1D Burger?s equation, and two test cases for the compressible Euler equations: a rising thermal bubble and density current. The results indicate that the proposed DG-localized Laplacian artificial viscosity method works robustly with a wide range of grid sizes and polynomial orders.

15. SUBJECT TERMS

16. SECURITY CLASSIFICATION OF:			17. LIMITATION OF ABSTRACT	18. NUMBER OF PAGES	19a. NAME OF RESPONSIBLE PERSON
a. REPORT **unclassified**	b. ABSTRACT **unclassified**	c. THIS PAGE **unclassified**	**Same as Report (SAR)**	**32**	

applied to 3D limited-area modeling on distributed-memory computers with a large number of processors [3, 4] as well as with adaptive mesh refinement (AMR) in 2D [5].

Despite the success in NH modeling by high-order accurate (i.e., order>2) methods [2, 6], robust and efficient stabilization of sharp flow gradients (e.g., thermal fronts) or flow discontinuities (e.g., shock) remains challenging in the design of high-order methods. Arguably, the two most frequently adopted methods to stabilize the high-order methods in the presence of non-smooth flow features are limiters, e.g., the total variation bounded (TVB) limiter in the numerical framework of Runge-Kutta discontinuous Galerkin (RKDG) [7], and artificial viscosity.

In the numerical simulation of nonhydrostatic mesoscale atmospheric modeling, very high-order polynomials can be used to approximate the solution, as shown in Reference [2]. Under this scenario, the implementation of limiters will be extremely time-consuming. Furthermore, after limiting, the solution might be represented by a lower-order or even piecewise constant reconstruction. This polynomial order reduction will dramatically increase the numerical dissipation of the DG algorithm in the neighborhood of the limited element. Sometimes, key flow features can be totally smeared out, especially on coarse meshes. Furthermore, some of the most effective positivity-preserving limiters are not shape-preserving [8]. Artificial viscosity provides an alternative way to handle high-order simulations on coarse (i.e., under-resolved) meshes in the presence of sharp fronts.

The idea of capturing shock wave discontinuities in a fluid by adding artificial viscosity into hyperbolic conservation laws originated from Von Neumann and Richtmyer [9] in 1950. Since then, many types of artificial viscosity methods have been developed to deal with flow discontinuity capturing. One crucial issue in all artificial viscosity modeling is how to describe the smoothness of the flow fields accurately. Smoothness indicators are used for this purpose. Different smoothness indicators have been designed based on the gradient of flow quantities (e.g., velocity, internal energy, etc.) [10, 11], the resolution of numerical representation [12, 13], the residual/entropy residual of simulation [14, 15, 16], and so on. Note that all these smoothness indicators can effectively localize the artificial viscosity in the vicinity of flow discontinuities. Based on the different procedures to design artificial diffusive terms and to incorporate them into the original governing equations, the artificial viscosity methods for computational fluid dynamics can be roughly classified into several categories. These include, but are not limited to

2

the streamline-upwind/Petrov-Galerkin (SUPG) type artificial viscosity [17, 18, 19, 20], localized artificial diffusivity using physical principles [10, 11, 21, 22, 23, 24, 25], the residual based artificial viscosity [14, 15, 26, 27, 28], the entropy artificial viscosity [16, 29, 30], the spectral vanishing viscosity [12, 31], and the Laplacian artificial viscosity [13, 32, 33, 34]. Other studies of the artificial viscosity methods can be found in References [35, 36, 37, 38, 39], just to name a few.

In this study, considering the features of the governing equations [2], we augment the original hyperbolic system with the localized Laplacian artificial diffusive terms [13]. As mentioned previously, the localized Laplacian artificial viscosity is reconstructed based on the smoothness of the flow fields. Therefore, an adequate amount of artificial viscosity is localized in the vicinity of sharp fronts to suppress the Gibbs oscillation. Meanwhile, vanishing artificial viscosity does not contaminate the smooth flow features away from sharp fronts.

The paper is organized as follows. The governing equations for the nonhydrostatic mesoscale atmospheric modeling and the discontinuous Galerkin discretization are introduced in Sec. 2. In Sec. 3, basic ideas behind the localized Laplacian artificial viscosity method are reviewed. A new family of modified Laplacian artificial viscosity models is introduced based on the proposed modeling principles. Sec. 4 then presents the numerical results from simulations of benchmark test cases. The sensitivity of free parameters in artificial viscosity modeling is also studied there. Finally, conclusions are summarized in Sec. 5.

2. Governing equations and discretization

Many different forms of the governing equations have been used for numerical weather prediction together with various numerical methods. For non-hydrostatic atmospheric modeling, three equations sets were presented in [2], namely, the non-conservative form using Exner pressure, momentum, and potential temperature (Set 1), the conservative form using density, momentum, and potential temperature (Set 2), and the conservative form using density, momentum, and total energy (Set 3). It was found in [2] that the two conservative forms outperform the non-conservative form. Therefore, we study equation Set 2 in this paper which is one of the equation sets used in the NUMA model [3, 4].

2.1 Governing equations

The 2D form of equation Set 2 reads

$$\frac{\partial Q}{\partial t} + \nabla \cdot \boldsymbol{F}(Q) = G(Q), \tag{1}$$

where $Q = (\rho, \rho u, \rho w, \rho \theta)$ are the conservative variables, ρ is the density, u and w are velocities in x and z directions, respectively, and θ the potential temperature. $\boldsymbol{F} = (f^x, f^z)$ is the inviscid flux and G is the source term. They are defined as

$$f^x = \begin{pmatrix} \rho u \\ \rho u^2 + p \\ \rho uw \\ \rho u\theta \end{pmatrix}, f^z = \begin{pmatrix} \rho w \\ \rho uw \\ \rho w^2 + p \\ \rho w\theta \end{pmatrix}, \text{ and } G = \begin{pmatrix} 0 \\ 0 \\ -\rho g \\ 0 \end{pmatrix} \tag{2}$$

where g is the gravitational constant, p is the pressure, and is related with θ by the equation of state as follows:

$$p = p_0 \left(\frac{\rho R\theta}{p_0} \right)^\gamma \tag{3}$$

where $\gamma = \frac{c_p}{c_v}$ is the ratio of specific heats (for constant pressure and constant volume), R is the gas constant, and p_0, is a reference pressure that is only a function of the vertical coordinate. Introducing the splitting of the density, pressure and potential temperature as $\rho = \rho_0 + \rho'$, $p = p_0 + p'$, and $\theta = \theta_0 + \theta'$, where the subscript '0' denotes the values in hydrostatic balance, we rewrite Eq. (1) as

$$\frac{\partial Q'}{\partial t} + \nabla \cdot \boldsymbol{F}'(Q) = G'(Q), \tag{4}$$

where $Q' = (\rho', \rho u, \rho w, \Theta')$, $\Theta = \rho\theta$ and $\Theta' = \Theta - \rho_0\theta_0$. Correspondingly, $\boldsymbol{F}'$ is written as

$$f^{x\prime} = \begin{pmatrix} \rho u \\ \rho u^2 + p' \\ \rho uw \\ \rho u\theta \end{pmatrix}, f^{y\prime} = \begin{pmatrix} \rho w \\ \rho uw \\ \rho w^2 + p' \\ \rho w\theta \end{pmatrix} \text{ and } G' = \begin{pmatrix} 0 \\ 0 \\ -\rho' g \\ 0 \end{pmatrix}. \tag{5}$$

The governing equations are solved on the physical domain Ω, which is partitioned into N non-overlapping elements Ω^i. The solution Q'_i on each element Ω^i belongs to $\mathbb{Q}^k(\Omega^i)$, where $\mathbb{Q}^k(\Omega^i)$ is the space of tensor product of polynomials of degree at most k in each variable defined on Ω^i. For conciseness, the element-wise continuous solution Q'_i is replaced with Q in the following sections when no confusion between Q'_i and Q_i is present. The same convention also applies to $\boldsymbol{F}'$ and G'.

2.2 Discontinuous Galerkin method

We approximate the exact solution of the conservation law using an element-wise continuous polynomial $Q_h \in V_h^{DG} = \{W \in L^2(\Omega^i)\}$. Let W be an arbitrary weighting function or test function from the same space V_h^{DG}. The weighted residual form of the governing equations on each element Ω^i then reads

$$\int_{\Omega^i} \frac{\partial Q_h}{\partial t} W dV + \int_{\Omega^i} \nabla \cdot \boldsymbol{F}(Q_h) W dV = \int_{\Omega^i} G(Q_h) W dV, \qquad \forall W \in V_h^{DG}. \tag{6}$$

Applying integration by parts to Eq. (6), one obtains

$$\int_{\Omega^i} \frac{\partial Q_h}{\partial t} W dV - \int_{\Omega^i} \nabla W \cdot \boldsymbol{F}(Q_h) dV + \int_{\partial\Omega^i} \boldsymbol{F} \cdot \boldsymbol{n} W dS = \int_{\Omega^i} G(Q_h) W dV, \tag{7}$$

where $\boldsymbol{F} = (f, g)$ and $\boldsymbol{n}$ is the outward unit normal vector of $\partial\Omega^i$.

It is clear that the surface integral in Eq. (7) is not properly defined as the numerical solution is discontinuous across element interfaces. In order to ensure conservation, the normal flux term $\boldsymbol{F} \cdot \boldsymbol{n}$ is replaced with a Riemann flux $F_{com}^n(Q_h^i, Q_h^{i+}, \boldsymbol{n})$, where Q_h^{i+} denotes the solution outside the current element Ω^i. Various (approximate) Riemann solvers can be used to calculate the Riemann flux, and the Rusanov Riemann solver is adopted in this paper. Then Eq. (7) can be rewritten as

$$\int_{\Omega^i} \frac{\partial Q_h}{\partial t} W dV - \int_{\Omega^i} \nabla W \cdot \boldsymbol{F}(Q_h) dV + \int_{\partial\Omega^i} F_{com}^n(Q_h^i, Q_h^{i+}, \boldsymbol{n}) W dS = \int_{\Omega^i} G(Q_h) W dV. \tag{8}$$

In the DG approach, a finite-dimensional basis set $\{W_j\}$ is chosen as the solution space. Then the governing equation is projected onto each member of the basis set. Thus, Eq. (8) is reformulated as

$$\frac{\partial}{\partial t} \int_{\Omega^i} W_k \sum_j (Q_{h,j} W_j) dV - \int_{\Omega^i} \nabla W_k \cdot \boldsymbol{F}(Q_h) dV + \int_{\partial\Omega^i} W_k F_{com}^n dS$$
$$= \int_{\Omega^i} W_k \sum_j (G_j W_j) dV. \tag{9}$$

Applying integration by parts again to the second term of Eq. (9), the strong form is obtained as

$$\frac{\partial}{\partial t} \int_{\Omega^i} W_k \sum_j (Q_{h,j} W_j) dV + \int_{\Omega^i} W_k \nabla \cdot \boldsymbol{F}(Q_h) dV + \int_{\partial\Omega^i} W_k (F_{com}^n - F^n) dS \tag{10}$$

$$= \int_{\Omega^i} W_k \sum_j (G_j W_j) \, dV,$$

where $F^n = \boldsymbol{F} \cdot \boldsymbol{n}$ is the local flux projected on $\partial\Omega^i$ in the surface normal direction.

The first integral in Eq. (10) is usually written as a multiplication of the mass matrix M and the time derivative of the solution vector $[Q_h]$. The square bracket '[]' denotes the vector form of the solution Q_h. The entries of the mass matrix M are of the form

$$M_{(k,j)} = \int_{\Omega^i} W_k W_j \, dV. \tag{11}$$

If $\boldsymbol{F}$ is a linear function of Q, then $\boldsymbol{F}$ can be expressed as $\boldsymbol{F} = \sum_j \boldsymbol{F}_j W_j$. Under this constraint, the second integral in Eq. (10) can be formulated as a multiplication of the stiffness matrix S^l and the flux vector F^l. The entries of the stiffness matrix S^l are written as

$$S^l_{(k,j)} = \int_{\Omega^i} W_k \frac{\partial W_j}{\partial x^l} \, dV \,, l = 1,2. \tag{12}$$

However, if $\boldsymbol{F}$ is a nonlinear function of Q, then $\boldsymbol{F}$ cannot generally be expressed via the basis set $\{W_j\}$. Quadratures are used to compute the volume and surface integrals. Clearly these operations can be expensive, and some cost-effective approaches are required to improve the computational efficiency. One such solution is the quadrature-free approach proposed in [40]. In this approach, it is assumed that the flux $\boldsymbol{F}$ is a polynomial which belongs to the same space $\mathbb{Q}^k(\Omega^i)$ as that of the solution Q_h, and denote it by $\boldsymbol{F}_h$. Then Eq. (10) still holds for $\boldsymbol{F}_h$.

We also assume that F^n_{com} belongs to the polynomial space $P^k(\partial\Omega^i)$ and can be expressed by the basis set $\{W_{f,j}\}$ as $F^n_{com,f} = \sum_j F^n_{com,f,j} W_{f,j}$ on each surface. Thus mass matrices B_f for the surface integration in Eq. (10) can be formed with entries

$$B_{f,(k,j)} = \int_f W_k W_{f,j} \, dS_f. \tag{13}$$

Substituting Eqs. (11) – (13) into Eq. (10), we obtain the following vector form

$$\frac{\partial[Q_h]}{\partial t} = -\sum_{l=1}^2 (M^{-1} S^l)[F^l] - \sum_f (M^{-1} B_f)\big[F^n_{com,f} - F^n_f\big] + [G_h]. \tag{14}$$

Now consider the nodal type allocation of degrees of freedom (DOFs) [41], and assume that W_m is the Lagrange polynomial, which satisfies $W_m(\boldsymbol{r}_j) = \delta_{mj}$, where $\boldsymbol{r}_j = (x_j, z_j)$ is the nodal point. Following Ref. [41], we introduce the differentiation matrix D_{x^l}, with the entries

$$D_{x^l,(j,m)} = \frac{\partial W_m}{\partial x^l}\bigg|_{r_j}. \tag{15}$$

Then the entries of MD_{x^l} can be calculated as

$$\left(MD_{x^l}\right)_{(k,m)} = \sum_j \int_{\Omega^i} W_k W_j \frac{\partial W_m}{\partial x^l}\bigg|_{r_j} dV = \int_{\Omega^i} W_k \sum_j W_j \frac{\partial W_m}{\partial x^l}\bigg|_{r_j} dV$$

$$= \int_{\Omega^i} W_k \frac{\partial W_m}{\partial x^l} dV = (S^l)_{(k,m)} \tag{16}$$

Therefore, Eq. (14) can be rewritten as

$$\frac{\partial[Q_h]}{\partial t} = -\sum_{l=1}^{2} D_{x^l}[F^l] - \sum_f (M^{-1}B_f)[F_{com,f}^n - F_f^n] + [G_h]. \tag{17}$$

According to Eq. (17), in the implementation of the strong form, there is no need to explicitly calculate the stiffness matrix S^l, but the differentiation of the flux polynomials. This fact can be utilized to save computational cost. More detailed information about this implementation can be found in Ref. [2].

3. Localized Laplacian artificial viscosity

The Laplacian artificial viscosity is used to suppress the Gibbs oscillation near sharp thermal fronts. Generally, for 2D problems, the Laplacian diffusion terms $\nabla \cdot \boldsymbol{F}^{av}(Q, \nabla Q)$ in x and z directions read

$$f^{av} = \begin{pmatrix} 0 \\ \varepsilon_{e,x}\rho \frac{\partial u}{\partial x} \\ \varepsilon_{e,x}\rho \frac{\partial w}{\partial x} \\ \varepsilon_{e,x}\rho \frac{\partial \theta'}{\partial x} \end{pmatrix} \text{ and } g^{av} = \begin{pmatrix} 0 \\ \varepsilon_{e,z}\rho \frac{\partial u}{\partial z} \\ \varepsilon_{e,z}\rho \frac{\partial w}{\partial z} \\ \varepsilon_{e,z}\rho \frac{\partial \theta'}{\partial z} \end{pmatrix}. \tag{18}$$

For simplicity, we set $\varepsilon_{e,x} = \varepsilon_{e,z} = \varepsilon_e$.

The DG method is used to discretize the following equivalent system of Eq. (4),

$$\vec{S} - \nabla Q = 0,$$

$$\frac{\partial Q}{\partial t} + \nabla \cdot \vec{F}^{inv}(Q) - \nabla \cdot \vec{F}^{av}(Q, \vec{S}) = G(Q). \tag{19}$$

Herein, $\vec{S}$ is the auxiliary variable to facilitate the discretization of viscous fluxes.

The artificial viscosity ε is modeled following the approach in Ref. [13]. Several modifications are introduced to make this model more suitable for sharp thermal front capturing in non-hydrostatic atmospheric modeling. In this study, the resolution-based indicator is used to detect non-smooth flow features. Specifically, we approximate the solution in the polynomial space $\mathbb{Q}^k(\Omega)$ as follows,

$$Q \approx U = \sum_{i=1}^{N(k)} U_i \phi_i, \tag{20}$$

where U is the polynomial approximation of Q, ϕ_i is the ith basis of the space $\mathbb{Q}^k(\Omega)$, and $N(k)$ is the total number of basis of $\mathbb{Q}^k(\Omega)$; for 2D problems, $N(k) = (k+1) \times (k+1)$.

Now we project the solution U onto the polynomial space $\mathbb{Q}^{k-1}(\Omega)$, and obtain

$$U^p = \sum_{i=1}^{N(k-1)} \widehat{U}_i \widehat{\phi}_i. \tag{21}$$

The expansion coefficients $\widehat{U}_i$ can be calculated by solving the following linear system,

$$\sum_{m=1}^{N(k-1)} \widehat{U}_m \langle \widehat{\phi}_m, \widehat{\phi}_j \rangle = \sum_{m=1}^{N(k)} U_m \langle \phi_m, \widehat{\phi}_j \rangle, \qquad j = 1, \cdots, N(k-1). \tag{22}$$

Note that $\langle \cdot, \cdot \rangle$ indicates the inner product in $L_2(\Omega)$.

The resolution-based indicator in one finite element can then be defined as

$$S_e = log_{10} \frac{\langle U - U^p, U - U^p \rangle_e}{\langle U, U \rangle_e}. \tag{23}$$

Finally, a smooth variation of the element-wise artificial viscosity ε_e is reconstructed as follows,

$$\varepsilon_e = \begin{cases} 0 & if\ S_e < S_0 - \kappa \\ \dfrac{\varepsilon_0}{2}\left(1 + sin\dfrac{\pi(S_e - S_0)}{2\kappa}\right) & if\ S_0 - \kappa \leq S_e \leq S_0 + \kappa \\ \varepsilon_0 & if\ S_e > S_0 + \kappa. \end{cases} \tag{24}$$

It is clear that $\varepsilon_e \in [0, \varepsilon_0]$. Note that S_0 in Eq. (24) is the estimated value of the smoothness indicator S_e for smooth flow features. According to Ref. [13], if the polynomial expansion has a similar behavior to the Fourier expansion, the smoothness indicator will be proportional to $-4log_{10}(k)$. Based on our analyses, this estimation can add unnecessary numerical dissipation to relatively smooth flow features. Therefore, S_0 is set as $-3log_{10}(k)$ in this study. The parameter κ determines the smoothness range on which the artificial viscosity functions.

Generally, κ needs to be chosen sufficiently large so as to ensure a sharp front capturing with smooth transition to flow fields nearby. It is found that κ can affect the performance of artificial viscosity more than the other parameters in Eq. (24) do. More test results on this parameter will be discussed in the following section.

Different from the modeling approach presented in Ref. [13], the artificial viscosity ε_0 is modeled as follows. First we recall the definition of the $Péclet$ number Pe for a diffusion process,

$$Pe = \frac{LU}{\alpha},$$

(25)

where U is the characteristic speed, L the characteristic length, and α the diffusion coefficient. The artificial viscosity ε_0 is proportional to α. In Refs. [13, 32], U is set as the maximum absolute value of the characteristic speed $|\lambda|_{max}$. L is the sub-cell grid size h/P, where h is the element size, and P is the polynomial order. ε_0 is set to be equivalent to α.

In this work, different models to bridge ε_0 and α are proposed to make the modeling of the artificial viscosity ε_0 less sensitive to the element size and polynomial order. The principles followed in this approach include:

- The artificial viscosity ε_0 is non-negative;
- When the resolution of the numerical scheme is infinite, i.e., $h \to 0$ or $P \to \infty$, the artificial viscosity $\varepsilon_0 \to 0$;
- The modeling is compatible with the classic results from the 2nd order accurate (or equivalently P^1 reconstruction) methods.

Instead of using the uniform assumption of the sub-cell grid size h/P, we redefine the length scale in Eq. (25) as the maximum distance between two adjacent quadrature points in the element, which is written as $\Delta h_{max} = \Delta \xi_{max} \cdot h$, where $\Delta \xi_{max}$, scaled in $[0,1]$, is the maximum distance between two adjacent quadrature points in a standard 1D element. Thus, α reads

$$\alpha = \frac{\Delta \xi_{max}}{Pe} \cdot h \cdot |\lambda|_{max}.$$

(26)

A general model for the artificial viscosity ε_0 can then be written as

$$\varepsilon_0 = f(\Delta \xi_{max}) \cdot h \cdot |\lambda|_{max}.$$

(27)

We now focus on the modeling of the non-dimensional function $f(\Delta \xi_{max})$. Following Ref. [37], we require that when the P^1 reconstruction is used, the function f passes the point

$(1,1/Pe)$. This is consistent with the definition of α for the 2nd order finite volume method. Then we show one way to determine a region of the function f that can satisfy the proposed modeling criteria. It is observed that one possible upper bound of the function f can be written as

$$f(\Delta\xi_{max}) = -\frac{1}{Pe}log\Delta\xi_{max} + \frac{1}{Pe}, \qquad \Delta\xi_{max} \in [0,1] \qquad (28)$$

It is not difficult to verify that $f(\Delta\xi_{max}) > 0$; if $\Delta\xi_{max}, h \to 0$, then $\varepsilon_0 \to 0$; and $f(\Delta\xi_{max})$ passes the point $(1,1/Pe)$. One possible lower bound of the function f can be expressed as

$$f(\Delta\xi_{max}) = \begin{cases} 0, & 0 \le \Delta\xi_{max} < 1 \\ \dfrac{1}{Pe}, & \Delta\xi_{max} = 1 \end{cases}. \qquad (29)$$

This region is shown in Figure 1 as the shadowed area. Note that the linear function $f(\Delta\xi_{max}) = \Delta\xi_{max}/Pe$ recovers the choice in Ref. [13, 32]. Based on our tests, the linear distribution

$$f(\Delta\xi_{max}) = -\frac{\Delta\xi_{max}}{Pe} + \frac{2}{Pe} \qquad (30)$$

is used to relate ε_0 with α. Finally, the artificial viscosity ε_0 is defined as

$$\varepsilon_0 = \left(-\frac{\Delta\xi_{max}}{Pe} + \frac{2}{Pe}\right) \cdot h \cdot |\lambda|_{max}. \qquad (31)$$

We note that the artificial viscosity ε_e given in Eq. (24) is an element-wise constant distribution. It is obvious that ε_e has a jump on element interfaces if the element-wise constant distribution is used. For quadrilateral elements, a bilinear distribution can be constructed by interpolating the four vertex artificial viscosity values to the desired quadrature points. The value of artificial viscosity on a specific vertex is calculated by averaging all values from the neighboring elements which share the vertex.

4. Results and discussions

In this section, we test the localized Laplacian artificial viscosity method using several benchmark problems with the presence of shock waves or sharp thermal fronts. In order to evaluate the performance of artificial viscosity on grids with different resolution, a wide range of grid sizes and polynomial orders is tested in each problem. In all simulations, S_0 in Eq. (24) is selected as $-3log_{10}(k)$ and the $Péclet$ number Pe is fixed at 2.

4.1 1D Burger's equation tests

In this section, we test the efficacy of the localized artificial viscosity for the 1D Burger's equation. The 1D inviscid Burger's equation augmented by an artificial diffusive term reads:

$$\frac{\partial U}{\partial t} + \frac{\partial}{\partial x}\left(\frac{1}{2}U^2\right) + \frac{\partial}{\partial x}\left(\varepsilon_e \frac{\partial U}{\partial x}\right) = 0, \tag{32}$$

where $x \in [-1,1]$. Periodic boundary conditions are enforced at $x = -1$ and $x = 1$. The initial conditions are defined as $U(x,0) = U_0(x) = 1 + \sin(\pi x)/2$. According to Reference [42], a moving shockwave will develop after $t = 2/\pi$ under the given initial conditions. An element-wise constant distribution of ε_e is used to stabilize the shock wave. In all simulations presented in this section, κ is chosen as 6.

First of all, the results of different artificial viscosity models presented in Section 3 are compared. The results are shown in Figure 2. In Fig. 2, 'Log' denotes the case with $f(\Delta\xi_{max}) = (1 - log\Delta\xi_{max})/Pe$; 'Linear(-)' the case with $f(\Delta\xi_{max}) = (2 - \Delta\xi_{max})/Pe$; 'Constant' the case with $f(\Delta\xi_{max}) = 1/Pe$; and 'Linear(+)' the case with $f(\Delta\xi_{max}) = \Delta\xi_{max}/Pe$. Simulations with both P^3 and P^8 reconstructions on ten elements are carried out. From Fig. 2, we observe that the model 'Log' is the most dissipative method and the model 'Linear(+)' is the least dissipative. It is also clear that the performance of the model 'Linear(+)' is sensitive to the polynomial order, while that of the other models is not. Based on this observation, the model 'Linear(-)' will be exclusively used in all simulations in the rest of the paper.

Next we compare the results with P^3 and P^8 reconstruction on different grids. The solutions at $t = 1$ are presented in Fig. 3. The corresponding local solution errors with respect to the exact solution of the inviscid Burger's equation at $t = 1$ are plotted in Fig. 4. Several observations are summarized as follows. From Fig. 3, we find that the localized artificial viscosity works robustly for a wide range of high-order reconstruction (e.g., from P^3 to P^8 in the current test). For all cases, the shock is captured in one element. From Figs. 4 and 5, it is clear that the localized artificial viscosity does not contaminate the smooth flow features away from the shock, but merely concentrates in the non-smooth flow regions to suppress the Gibbs oscillation. From Fig. 5, we observe that as the resolution of the numerical scheme becomes finer (i.e., the element size becomes smaller or the order of the reconstruction polynomial becomes higher), the amount of artificial viscosity localized in the vicinity of the shock wave becomes smaller. This follows the modeling rules as stated in Sec. 3.

4.2 Rising thermal bubble

The rising thermal bubble problem is driven by buoyancy effects. Specifically, a dry warm bubble rises in a constant potential temperature environment, and interacts with the ambient air during this process. The initial potential temperature perturbation is given as follows [2]:

$$\theta' = \begin{cases} 0 & if\ r > r_c, \\ \dfrac{\theta_c}{2}\left[1 + cos\left(\dfrac{\pi r}{r_c}\right)\right] & if\ r \le r_c, \end{cases} \tag{33}$$

where $\theta_c = 0.5^o C$, $r_c = 250m$, $r = \sqrt{(x - x_c)^2 + (z - z_c)^2}$, and $(x_c, z_c) = (500, 300)\ m$ is the initial geometric center of the bubble. The hydrostatic potential temperature θ_0 for this case is $300K$. The simulation domain is $(x, z) \in [0,1000]^2\ m$. The thermal bubble evolves until $t = 700s$. Four resolutions, namely, 20m, 10m, 5m and 3.5m, as presented in [2], are adopted in the simulations. The resolution is defined as $L/(n_{grid} \times k)$, where L is the domain size in the x or z direction, n_{grid} is the number of elements in the corresponding direction, and k is the polynomial order. Unless explicitly specified, κ in the artificial viscosity model is set as 0.5 in all simulations presented in this section.

4.2.1 Results from localized artificial viscosity

The maximum and minimum potential temperature perturbations θ'_{max} and θ'_{min} at $t = 700$s with various flow field resolutions are presented in Fig. 6. Note that since initially $\theta' \in [0, 0.5]$, it is then expected that during the evolution of the thermal bubble, θ' is bounded in this range. From Figure 6, it is found that the localized Laplacian artificial viscosity functions perform well for a wide range of grid sizes and polynomial orders. Only small overshoots of potential temperature perturbation show up in the results. As the resolution of flow fields becomes finer, the numerical dissipation becomes smaller. Correspondingly, both maximum and minimum potential temperature perturbations approach the theoretical bounds.

Then the effects of κ on flow field features are studied with P^{10} reconstruction on a 20×20 mesh (i.e., the resolution is 5m). The potential temperature perturbation fields with different κ, namely, 0.5, 1, 2, 3, and 4, are shown in Fig. 7. It is observed that as κ increases, the plume-like flow features near the thermal front are gradually damped. From the maximum and minimum

potential temperature perturbations θ'_{max} and θ'_{min} at $t = 700$s as tabulated in Table 1, it is clear that the overshoot of θ'_{min} for all cases is very small, and decreases quickly as κ increases.

The mass and energy conservation properties are studied for low resolution cases, including both 20m and 10m cases. The mass and energy are defined as

$$M(t) = \int_{\Sigma \Omega^i} \rho(t) dV \quad and \ E(t) = \int_{\Sigma \Omega^i} \rho(t) e(t) dV, \tag{34}$$

where e is the total energy. In this case, e is calculated as $\frac{p}{\gamma - 1} + \frac{1}{2}(u^2 + v^2)$. Correspondingly, the mass and energy loss are defined as

$$M\_Loss(t) = \left| \frac{M(t) - M(0)}{M(0)} \right| \quad and \ E\_Loss(t) = \left| \frac{E(t) - E(0)}{E(0)} \right|. \tag{35}$$

The results for P^{10} solution reconstruction on both 5×5 and 10×10 meshes are shown in Fig. 8. It is found that the localized artificial viscosity can ensure mass conservation and only dissipates internal energy which is to be expected since the artificial viscosity used here is not meant to represent the proper Navier-Stokes viscous stress terms.

4.2.2 Comparison between localized artificial viscosity and limiters

To examine the advantage of the localized artificial viscosity method on handling various high-order simulations on coarse meshes, the rising thermal bubble case is run with low resolution (i.e., 20m and 10m) using both P^3 and P^{10} reconstruction. The results are then compared with those from a limiter using the combined hierarchical moment limiting procedure [43] and accuracy-preserving positivity limiting procedure [8].

A minmod TVB (total-variation-bounded) marker based on the potential temperature θ' is used to detect the "troubled" cell in the hierarchical moment limiting procedure. For "troubled" quadrilateral elements, a tensor product of the 1D mean-preserving basis [43] is used to carry out the solution reconstruction. The maximum polynomial order for the solution reconstruction in the "troubled" cells is fixed at two (i.e., 3rd order accurate). In the accuracy-preserving positivity limiting process, the potential temperature θ' in the element with negative θ' is limited as follows

$$\widehat{\theta'} = \alpha(\theta' - \overline{\theta'}) + \overline{\theta'}, \tag{36}$$

where $\alpha = \frac{\overline{\theta'}-\varepsilon}{\overline{\theta'}-\theta'_{min}}$, $\overline{\theta'}$ is the cell-averaged value, $\theta'_{min} = min_{j\in S(\Omega_e)}\theta'_j$, $S(\Omega_e)$ is the set of indices of all quadrature points in element Ω_e, and ε is a small positive number (e.g., 10^{-16} in this study). More details about the implementation of the two limiting procedures can be found in [8, 43].

The potential temperature perturbation fields at $700s$ from simulations using localized artificial viscosity or limiters on the coarse mesh with resolution of 20m are displayed in Fig. 9. P^3 solution reconstruction is used for (a) and (c) with localized artificial viscosity and limiters, respectively; P^{10} solution reconstruction is used for (b) and (d) with localized artificial viscosity and limiters, respectively. To ensure the same resolution for all simulations, a 17×17mesh is used for P^3 reconstruction, and 5×5 for P^{10} reconstruction. From this figure, we observe that the flow fields using localized artificial viscosity are much smoother than those using limiters. The results using P^{10} solution reconstruction with P^2 limiting procedure cannot preserve the shape of the rising thermal bubble. Similar conclusions can be drawn from Fig. 10, which shows the potential temperature perturbation fields at $700s$ with similar numerical setup as that in Fig. 9, but a 34×34 mesh for P^3 reconstruction and 10×10 for P^{10} reconstruction (i.e., the resolution is 10m). All these results demonstrate the superior properties of localized artificial viscosity on stabilizing flows with thermal fronts for a wide range of polynomial orders and grid sizes.

4.2.3 Comparison between localized artificial viscosity and constant viscosity

Currently a common practice to suppress Gibbs oscillation in thermal front capturing is to add constant viscosity [44] to the governing equations. Specifically, the physical viscous diffusion term $\nabla \cdot \boldsymbol{F}^v(Q, \nabla Q)$ is added to the right-hand side of Eq. (4). $\boldsymbol{F}^v(Q, \nabla Q)$ in x and z directions can be written as

$$f^v = \begin{pmatrix} 0 \\ \mu\rho\frac{\partial u}{\partial x} \\ \mu\rho\frac{\partial w}{\partial x} \\ \mu\rho\frac{\partial \theta}{\partial x} \end{pmatrix} \text{ and } g^v = \begin{pmatrix} 0 \\ \mu\rho\frac{\partial u}{\partial z} \\ \mu\rho\frac{\partial w}{\partial z} \\ \mu\rho\frac{\partial \theta}{\partial z} \end{pmatrix}, \tag{37}$$

where μ is the constant viscosity.

It is obvious that this approach adds numerical dissipation to the entire flow field, no matter whether the local flow features are smooth or not. The potential temperature perturbation fields

at $700s$ for P^{10} solution reconstruction on a $10{\times}10$ mesh using a series of constant viscosity, namely, $0.1\text{m}^2/\text{s}$, $0.2\text{m}^2/\text{s}$, $0.3\text{m}^2/\text{s}$, $0.5\text{m}^2/\text{s}$, $1\text{m}^2/\text{s}$ and $2\text{m}^2/\text{s}$, are presented in Fig. 11. The corresponding maximum and minimum potential temperature perturbations θ'_{max} and θ'_{min} at $t = 700\text{s}$ using localized artificial viscosity and constant viscosity are tabulated in Table 2. From these results, we observe that for the rising thermal bubble case, the performance of constant viscosity with $\mu = 0.2\text{m}^2/\text{s}$ is very similar to that of localized artificial viscosity as shown in Fig. 10(d). If the constant viscosity is very large, e.g., $\mu = 2\text{m}^2/\text{s}$, as shown in Fig. 11(f), the flow structures can be severely dissipated. Although a $10{\times}10$ mesh is used, the resolution of the case with $\mu = 2\text{m}^2/\text{s}$ is very similar to the localized artificial viscosity case on a $5{\times}5$ mesh as show in Fig. 9(d). More advantages of the localized artificial viscosity approach over the constant viscosity approach will be presented in Sec. 4.3.2.

4.3 Density current

Now we study the density current problem. In this case, a cold bubble drops in a neutrally stratified atmosphere, hits the ground, and generates Kelvin–Helmholtz rotors. The initial potential temperature perturbation is given as follows [2]:

$$\theta' = \frac{\theta_c}{2}\left[1 + cos\left(\frac{\pi r}{r_c}\right)\right] \tag{38}$$

where $\theta_c = -15^oC$, $r_c = 1m$, $r = \sqrt{\left(\frac{x-x_c}{x_r}\right)^2 + \left(\frac{z-z_c}{z_r}\right)^2}$, $(x_c, z_c) = (0, 3000)\ m$ is the initial center of the bubble, and $(x_r, z_r) = (4000, 2000)\ m$. Similarly to the rising thermal bubble case, the hydrostatic potential temperature θ_0 is set to $300K$. The simulation domain is $(x, z) \in [0,25600]{\times}[0,6400]\ m$. The cold bubble evolves until $t = 900s$. Four resolutions, namely, 400m, 200m, 100m and 50m, are used in the simulations. In Ref. [2], a constant dynamic viscosity is used to ensure a grid-converged solution at approximately 50m resolution. Without explicit viscosity, the simulation will eventually blow up. We now present a flow feature based artificial viscosity to stabilize the simulation. Unless explicitly specified, κ in the artificial viscosity model is set as 1 in all simulations presented in this section.

4.3.1 Results from localized artificial viscosity

The maximum and minimum potential temperature perturbations θ'_{max} and θ'_{min} at $t = 900$s with various flow field resolutions are presented in Fig. 12. Similar conclusions can be drawn from this figure as those for the rising thermal bubble case. The localized Laplacian artificial viscosity works well in a wide range of grid sizes and polynomial orders.

The effects of κ on flow field features are studied with P^8 reconstruction on both 8×2 (i.e., 400m resolution) and 64×16 meshes (i.e., 50m resolution). The potential temperature perturbation fields with different κ, namely, 0.25, 0.5, and 1, on the coarse mesh, and those with $\kappa = 0.5, 1, 2, 4, 6$ on the fine mesh are displayed in Figs. 13 and 14, respectively. It is found that the artificial viscosity is very dissipative on the coarse mesh, even when a small κ is used. For the fine grid results, as κ increases, fewer Kelvin–Helmholtz rotors are generated. In Table 2, we tabulate the maximum and minimum potential temperature perturbations θ'_{max} and θ'_{min} at $t = 900$s for the fine grid results. It is clear from Table 2 that the overshoot of θ'_{max} for all cases is small, and decreases quickly as κ increases, especially when κ exceeds 2.

4.3.2 Comparison between localized artificial viscosity and constant viscosity

The potential temperature perturbation fields at $900s$ for P^8 solution reconstruction on a 16×4 mesh using localized artificial viscosity and a series of constant viscosity, namely, $50\text{m}^2/\text{s}$, $75\text{m}^2/\text{s}$, $100\text{m}^2/\text{s}$ and $125\text{m}^2/\text{s}$, are displayed in Fig. 15. The corresponding maximum and minimum potential temperature perturbations θ'_{max} and θ'_{min} at $t = 900$s using localized artificial viscosity and constant viscosity are tabulated in Table 4. A similar trend can be concluded as that in Sec. 4.2.3.

It is found that if the constant viscosity is "small", e.g., $\mu = 25\text{m}^2/\text{s}$, the simulation diverged. Note that $\mu = 2\text{m}^2/\text{s}$ is considered a "large" viscosity value in the rising thermal bubble case (This is true even if we consider the dimensionless parameter $\frac{\mu}{\Delta x^2}$). Therefore, from the comparison of these two cases, we conclude that the constant viscosity approach suffers from the large variation of viscosity for stabilization purpose. However, the value of localized artificial viscosity is determined by the numerical resolution of the scheme, and almost no parameter adjustment is needed in simulations of different problems. This is one big advantage of the localized artificial viscosity approach over the constant viscosity approach.

5. Conclusions

We present a coupled DG-localized Laplacian artificial viscosity method to suppress Gibbs oscillation near sharp thermal fronts in nonhydrostatic mesoscale atmospheric modeling. Specifically, the original inviscid governing equations are augmented by Laplacian artificial diffusive terms. The diffusivity is a function of the local smoothness of the flow fields. Thus, the proposed method has a favorable sub-cell shock capturing property, and does not contaminate the smooth flow features away from the non-smooth regions, as demonstrated by the simulation results for the 1D Burger's problem.

In order to alleviate the sensitivity of the free parameters in artificial viscosity modeling on both grid sizes and polynomial orders, a family of localized artificial viscosity models is proposed and tested. We use this numerical framework to simulate two classical 2D test cases from nonhydrostatic mesoscale atmospheric modeling, namely, rising thermal bubble and density current tests. The results using localized artificial viscosity are then compared with those using limiters and constant viscosity. The results show that the proposed artificial viscosity method works robustly with a wide range of grid sizes and polynomial orders.

References

[1] J. Steppeler, R. Hess, U. Schättler and L. Bonaventura, "Review of numerical methods for nonhydrostatic weather prediction models," *Meteorology and Atmospheric Physics,* vol. 82, pp. 287-301, 2003.

[2] F. X. Giraldo and M. Restelli, "A study of spectral element and discontinuous Galerkin methods for the Navier-Stokes equations in nonhydrostatic mesoscale atmospheric modeling: equations sets and test cases," *J. Comput. Phys.,* vol. 227, pp. 3849-3877, 2008.

[3] J. F. Kelly and F. X. Giraldo, "Continuous and discontinuous Galerkin methods for a scalable 3D nonhydrostatic atmospheric model: limited-area mode," *J. Comput. Phys.,* vol. 231, pp. 7988-8008, 2012.

[4] F. X. Giraldo, J. F. Kelly and E. M. Constantinescu, "Implicit-explicit formulations for a 3D nonhydrostatic unified model of the atmosphere (NUMA)," *SIAM J. Sci. Comp.,* vol. 35, no. 5, pp.

B1162-B1194, 2013.

[5] M. A. Kopera and F. X. Giraldo, "Analysis of adaptive mesh refinement for IMEX discontinuous Galerkin solutions of the compressible Euler equations with application to atmospheric simulations," *J. Comp. Phys.,* 2014, under revision.

[6] P. A. Ullrich and C. Jablonowski, "MCore: A non-hydrostatic atmospheric dynamical core utilizing high-order finite-volume methods," *J. Comp. Phys.,* vol. 231, pp. 5078-5108, 2012.

[7] B. Cockburn and C.-W. Shu, "The Runge–Kutta discontinuous Galerkin finite element method for conservation laws V: multidimensional systems," *J. Comput. Phys.,* vol. 141, pp. 199-224, 1998.

[8] X. Zhang and C.-W. Shu, "On positivity preserving high order discontinuous Galerkin schemes for compressible Euler equations on rectangular meshes," *Journal of Computational Physics,* vol. 229, pp. 8918-8934, 2010.

[9] J. Von Neumann and R. D. Richtmyer, "A method for the numerical calculation of hydrodynamic shocks," *J. Appl. Phys.,* vol. 21, pp. 232-237, 1950.

[10] A. W. Cook and W. H. Cabot, "A high-wavenumber viscosity for high-resolution numerical methods," *J. Comput. Phys.,* vol. 195, pp. 594-601, 2004.

[11] S. Kawai and S. Lele, "Localized artificial diffusivity scheme for discontinuity capturing on curvilinear meshes," *J. Comput. Phys.,* vol. 227, pp. 9498-9526, 2008.

[12] E. Tadmor, "Shock Capturing by the spectral viscosity method," *Comput. Methods Appl. Mech. Engrg.,* vol. 80, pp. 197-208, 1990.

[13] P.-O. Persson and J. Peraire, "Sub-Cell Shock Capturing for Discontinuous Galerkin Methods," in *44th AIAA Aerospace Sciences Meeting and Exhibit*, Reno, Nevada, 2006, AIAA-2006-0112.

[14] F. Bassi and S. Rebay, "Accurate 2D Euler computations by means of a high order discontinuous finite element method," in *XIVth ICN MFD*, Bangalore, India, 1994.

[15] R. Hartmann and P. Houston, "Adaptive discontinuous Galerkin finite element methods for the compressible Euler equations," *J. Comput. Phys.,* vol. 183, pp. 508-532, 2002.

[16] J.-L. Guermond and R. Pasquetti, "Entropy-based nonlinear viscosity for Fourier approximations of conservation laws," *C. R. Acad. Sci., Ser. I,* vol. 346, pp. 801-806, 2008.

[17] T. Hughes and M. Mallet, "A new finite element formulation for computational fluid dynamics . IV. A discontinuity-capturing operator for multidimensional advective-diffusive systems," *Comput. Methods Appl. Mech. Eng.,* vol. 58, pp. 329-336, 1986.

[18] T. E. Tezduyar and Y. J. Park, "Discontinuity-capturing finite element formulations for nonlinear convection-diffusion-reaction equations," *Comput. Methods Appl. Mech. Engrg.,* vol. 59, pp. 307-325, 1986.

[19] C. Johnson, A. Szepessy and P. Hansbo, "On the convergence of shock-capturing streamline diffusion finite element methods for hyperbolic conservation laws," *Math. Comput.,* vol. 54, pp. 107-129, 1990.

[20] T. E. Tezduyar and M. Senga, "Stabilization and shock-capturing parameters in SUPG formulation of compressible flows," *Comput. Methods Appl. Mech. Engrg.,* vol. 195, pp. 1621-1632, 2006.

[21] A. W. Cook, "Artificial fluid properties for large-eddy simulation of compressible turbulent mixing," *J. Comput. Phys.,* vol. 227, pp. 9498-9526, 2008.

[22] S. Kawai, S. K. Shankar and S. K. Lele, "Assessment of localized artificial diffusivity scheme for large-eddy simulation of compressible turbulent flows," *J. Comput. Phys.,* vol. 229, pp. 1739-1762, 2010.

[23] S. Premasuthan, C. Liang and A. Jameson, "Computation Of flows with shocks using spectral difference scheme with artificial viscosity," in *48th AIAA Aerospace Sciences Meeting Including the New Horizons Forum and Aerospace Exposition*, Orlando, Florida, 2010, AIAA-2010-1449.

[24] B. J. Olson and S. K. Lele, "Directional artificial fluid properties for compressible large-eddy simulation," *J. Comput. Phys.,* vol. 246, pp. 207-220, 2013.

[25] T. Haga and S. Kawai, "Toward accurate simulation of shockwave-turbulence interaction on unstructured meshes: a coupling of high-order FR and LAD schemes," in *21st AIAA Computational Fluid Dynamics Conference*, San Diego, CA, 2013, AIAA-2013-3065.

[26] F. Bassi, S. Rebay, G. Mariotti, S. Pedinotti and M. Savini, "A high-order accurate discontinuous finite element method for inviscid and viscous turbomachinery flows," in *2nd European Conference on Turbomachinery Fluid Dynamics and Thermodynamics*, Antwerpen, Belgium, 1997.

[27] R. Hartmann, "Adaptive discontinuous Galerkin methods with shock-capturing for the compressible Navier-Stokes equations," *Int. J. Numer. Meth. Fluids,* vol. 51, pp. 1131-1156, 2006.

[28] A. Kurganov and Y. Liu, "New adaptive artificial viscosity method for hyperbolic systems of conservation laws," *J. Comput. Phys.,* vol. 231, pp. 8114-8132, 2012.

[29] J.-L. Guermond, R. Pasquetti and B. Popov, "Entropy viscosity method for nonlinear conservation laws," *J. Comput. Phys.,* vol. 230, pp. 4248-4267, 2011.

[30] V. Zingan, J.-L. Guermond, J. Morel and B. Popov, "Implementation of the entropy viscosity method with the discontinuous Galerkin method," *Comput. Methods Appl. Mech. Engrg.,* vol. 253, pp. 479-490, 2013.

[31] A. A. Oberai and J. Wanderer, "A dynamic multiscale viscosity method for the spectral approximation of conservation laws," *Comput. Methods Appl. Mech. Engrg.,* vol. 195, pp. 1778-1792, 2006.

[32] G. E. Barter and D. L. Darmofal, "Shock capturing with PDE-based artificial viscosity for DGFEM: Part I. Formulation," *J. Comput. Phys.,* vol. 229, pp. 1810-1827, 2010.

[33] A. Klöckner, T. Warburton and J. S. Hesthaven, "Viscous shock capturing in a time-explicit discontinuous Galerkin method," *Math. Model. Nat. Phenom.,* vol. 6, pp. 57-83, 2011.

[34] P.-O. Persson, "Shock capturing for high-order discontinuous Galerkin simulation of transient flow problems," in *21st AIAA Computational Fluid Dynamics Conference*, San Diego, CA, 2013, AIAA-2013-3061.

[35] A. Jameson, "Analysis and design of numerical schemes for gas dynamics, 2: artificial diffusion and," *International Journal of Computational Fluid Dynamics,* vol. 5, pp. 1-38, 1995.

[36] E. J. Caramana, M. J. Shashkov and P. P. Whalen, "Formulations of artificial viscosity for multi-dimensional shock wave computations," *J. Comput. Phys.,* vol. 144, pp. 70-97, 1998.

[37] P. G. Huang, Z. J. Wang and Y. Liu, "An implicit space-time spectral difference method for discontinuity capturing using adaptive polynomials," in *17th AIAA Computational Fluid Dynamics Conference*, Toronto, Ontario, Canada, 2005, AIAA-2005-5255.

[38] T. V. Kolev and R. N. Rieben, "A tensor artificial viscosity using a finite element approach," *J. Comput. Phys.,* vol. 228, pp. 8336-8366, 2009.

[39] J. Reisner, J. Serencsa and S. Shkoller, "A space–time smooth artificial viscosity method for nonlinear conservation laws," *J. Comput. Phys.,* vol. 235, pp. 912-933, 2013.

[40] H. L. Atkins and C.-W. Shu, "Quadrature-free implementation of discontinuous Galerkin method for hyperbolic equations," *AIAA J.,* vol. 36, pp. 775-782, 1998.

[41] J. S. Hesthaven and T. Warburton, Nodal Discontinuous Galerkin methods: algorithms, analysis, and applications, New York: Springer-Verlag, 2008.

[42] A. Harten, B. Engquist, S. Osher and S. Chakravarthy, "Uniformly high order essentially non-oscillatory schemes III," *J. Comput. Phys.,* vol. 71, pp. 231-303, 1987.

[43] M. Yang and Z. Wang, "A Parameter-Free Generalized Moment Limiter for High-Order Methods on Unstructured Grids," *Advances in Applied Mathematics and Mechanics,* vol. 1, pp. 451-480, 2009.

19

[44] L. Yelash, A. Mueller, M. Lukacova-Medvidova, F. X. Giraldo and V. Wirth, "Adaptive discontinuous evolution Galerkin method for dry atmospheric flow," *J. Comput. Phys.,* vol. 268, pp. 106-133, 2014.
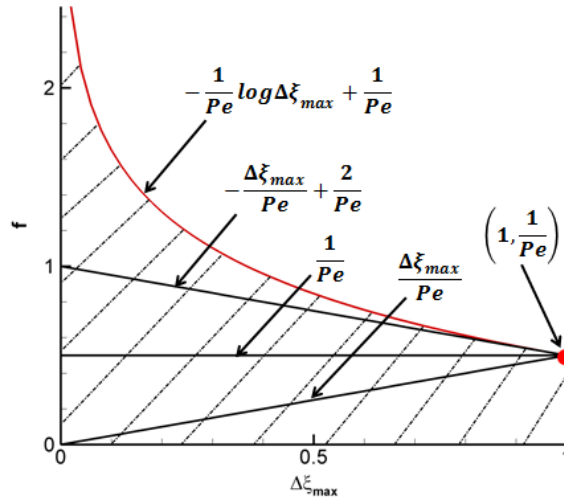
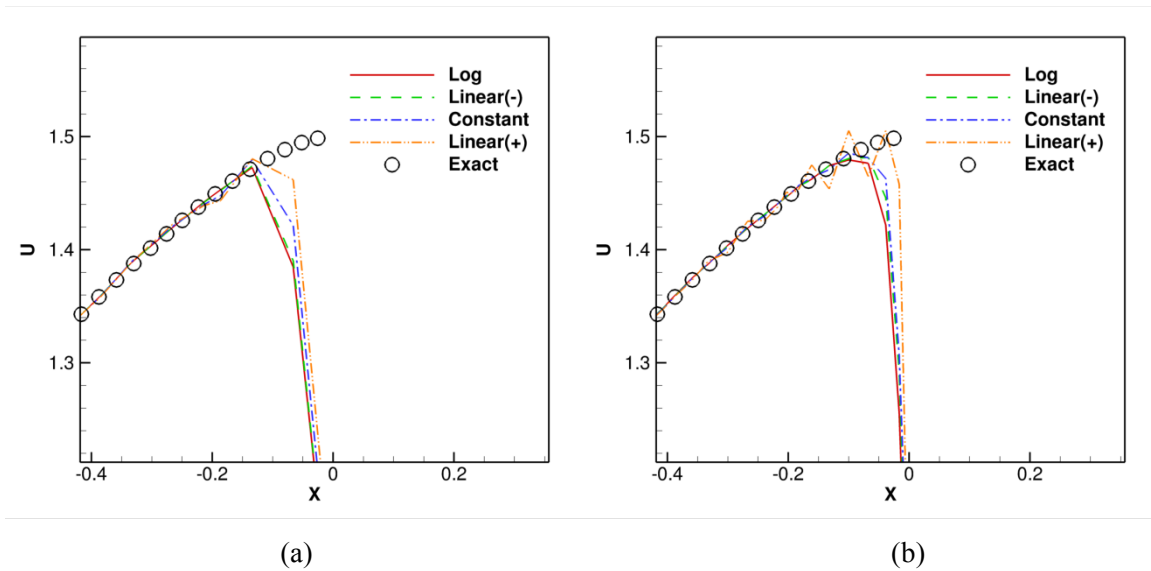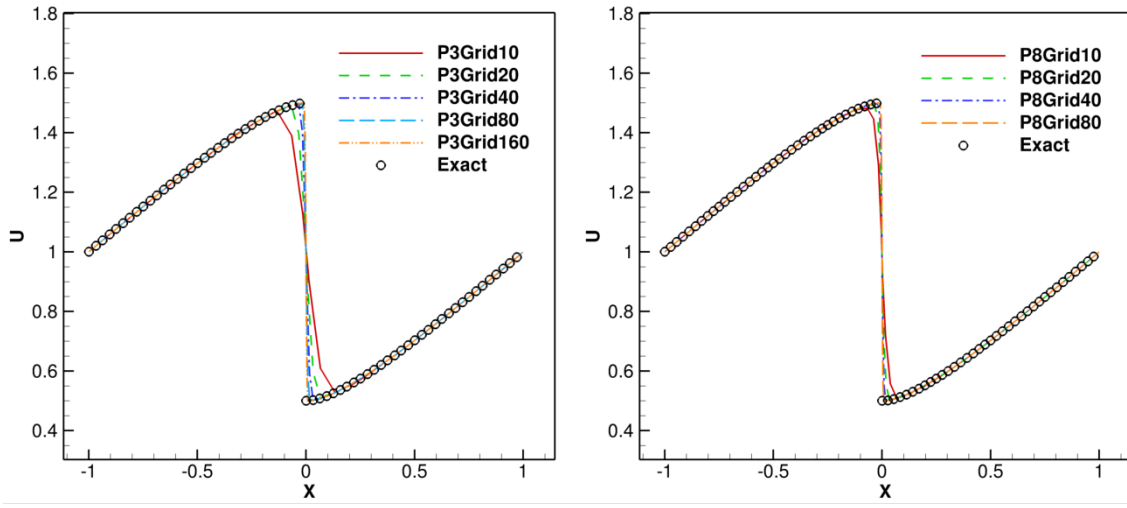**Figure 1.** Paradigm of the family of functions $f(\Delta\xi_{max})$ in the artificial viscosity model.

(a)   (b)

Figure 2. Zoom-in view of the solutions of the 1D Burger's equation near the shock wave with different artificial viscosity models at $t = 1$ on ten elements. (a) P^3 reconstruction; (b) P^8 reconstruction.

Figure 3. Solutions of the 1D Burger's equation at $t = 1$ on different grids. (a) P^3 reconstruction; (b) P^8 reconstruction.
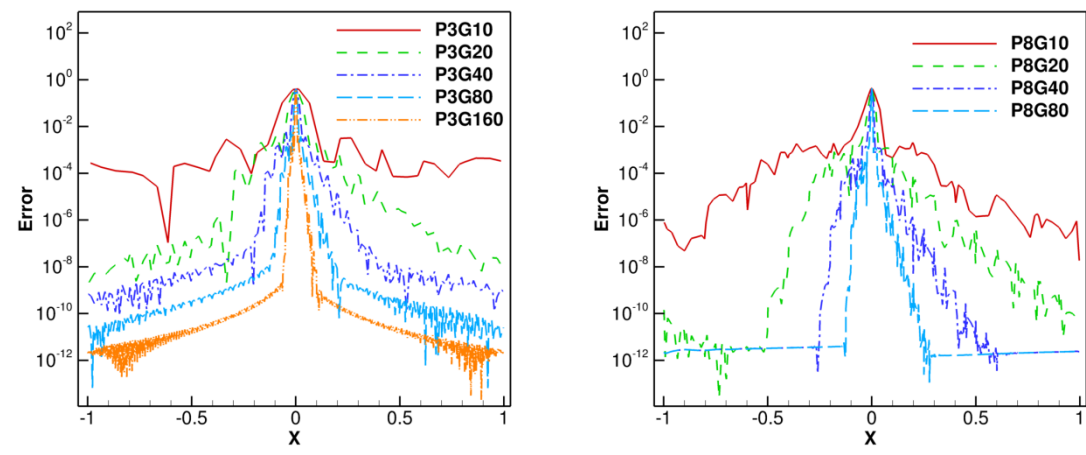
Figure 4. Local error of computed solutions of the 1D Burger's equation at $t = 1$ on different grids. (a) P^3 reconstruction; (b) P^8 reconstruction.

(a)   (b)
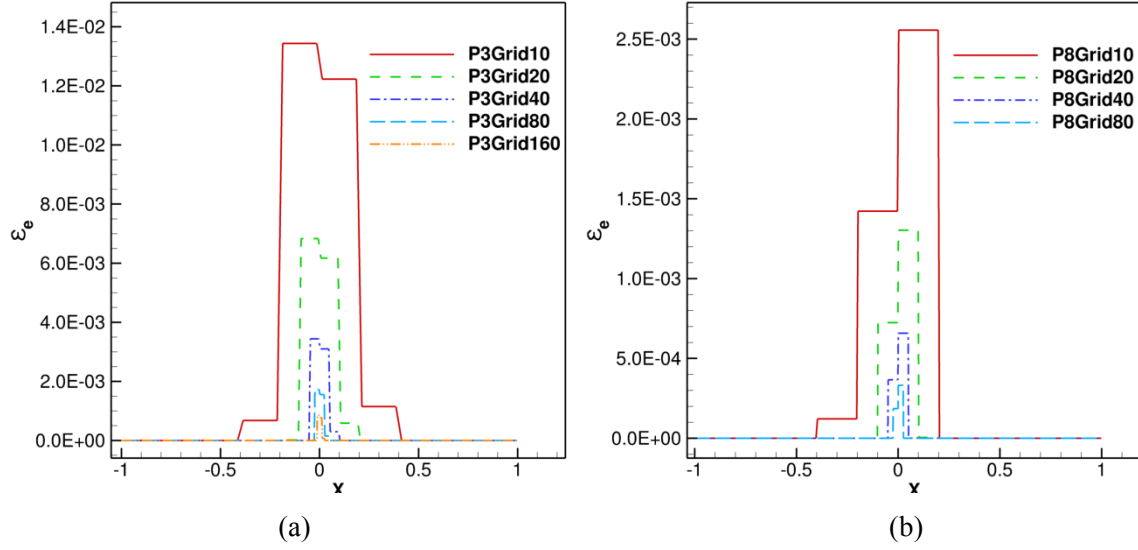
Figure 5. Distribution of the artificial viscosity from the 1D Burger's equation simulation at $t = 1$ on different grids. (a) P^3 reconstruction; (b) P^8 reconstruction.

(a)   (b)
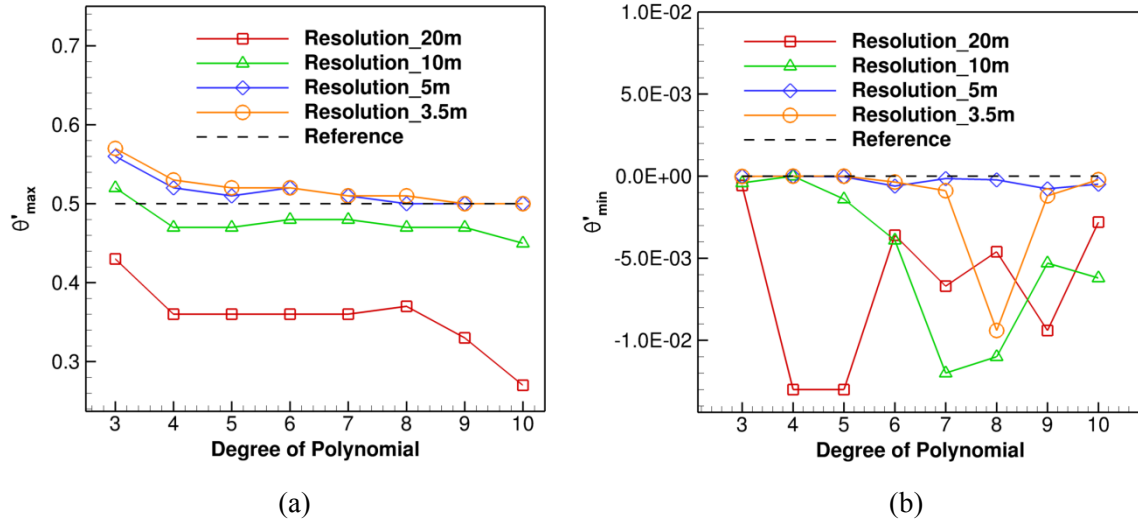
Figure 6. The maximum and minimum potential temperature perturbations θ'_{max} and θ'_{min} of the rising thermal bubble at $t = 700s$ with various flow field resolutions. (a) θ'_{max} vs. degree of polynomial; (b) θ'_{min} vs. degree of polynomial.
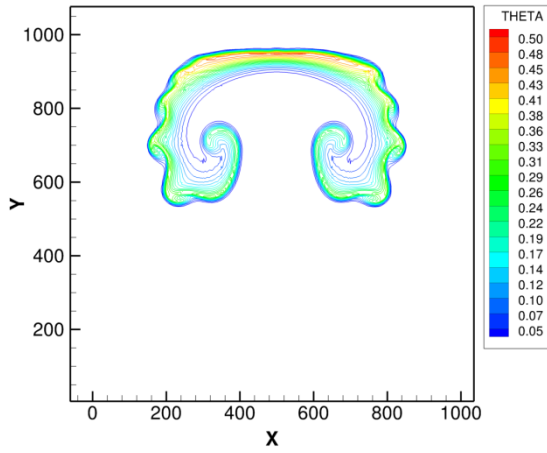
(a) $\kappa = 0.5$
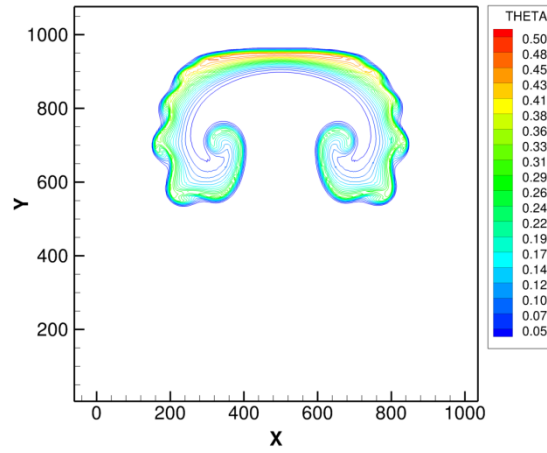
(b) $\kappa = 1$
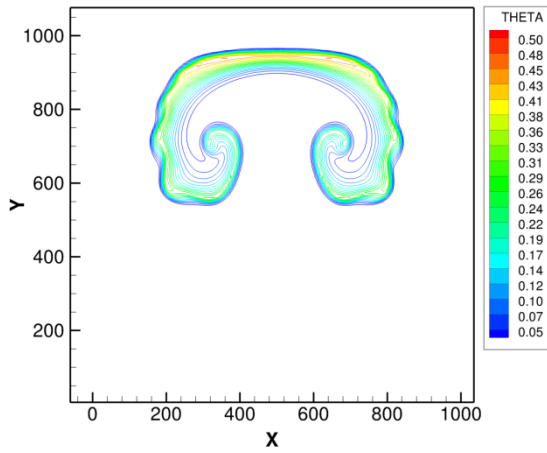
(c) $\kappa = 2$
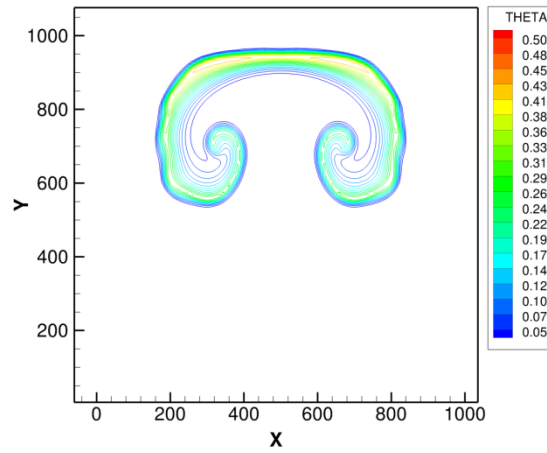
(d) $\kappa = 3$
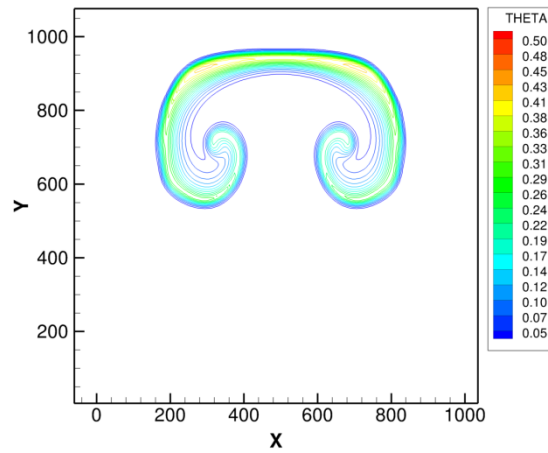
(e) $\kappa = 4$

Figure 7. Potential temperature perturbation fields of the rising thermal bubble at $t = 700s$ for different κ with P^{10} reconstruction on the 20×20 mesh.

κ	Max θ'	Min θ'
0.5	0.5049	-4.889×10^{-4}
1.0	0.4919	-2.972×10^{-4}
2.0	0.4774	-1.356×10^{-4}
3.0	0.4506	-4.311×10^{-5}
4.0	0.4381	-6.841×10^{-6}

Table 1. The maximum and minimum potential temperature perturbations θ'_{max} and θ'_{min} of the rising thermal bubble at $t = 700s$ for different κ with P^{10} reconstruction on a 20×20 mesh.

(a)　　　　　　　　　　　　　　　　(b)
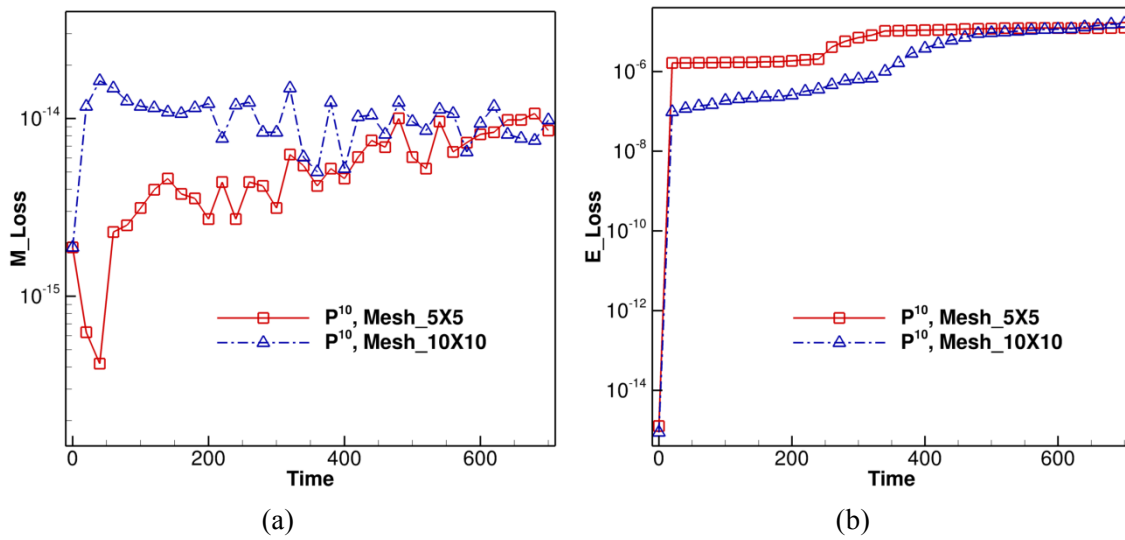
Figure 8. Conservation of (a) mass and (b) energy for the rising thermal bubble simulations using localized artificial viscosity on two different meshes with P^{10} reconstruction.

(a)　　　　　　　　　　　　　　　　(b)

(c)   (d)
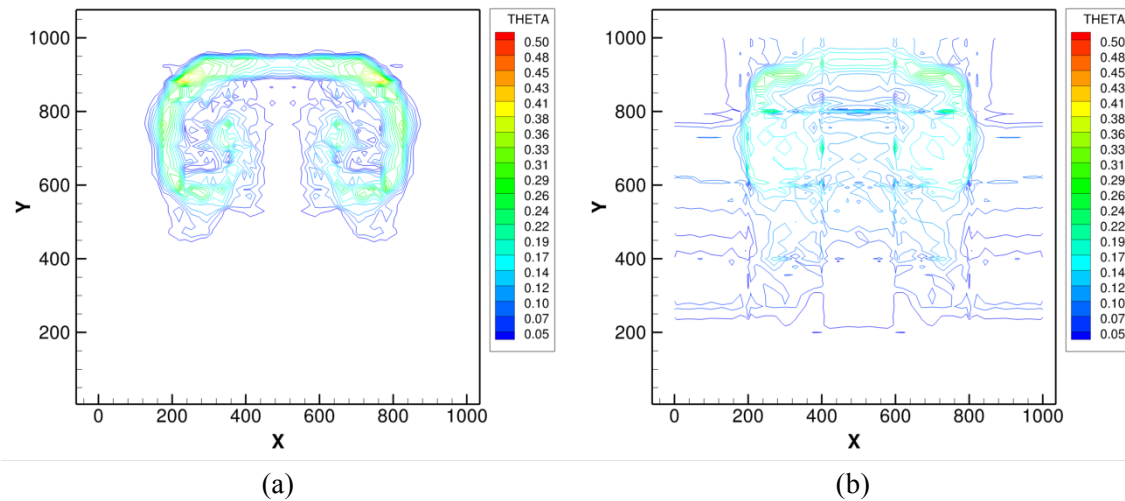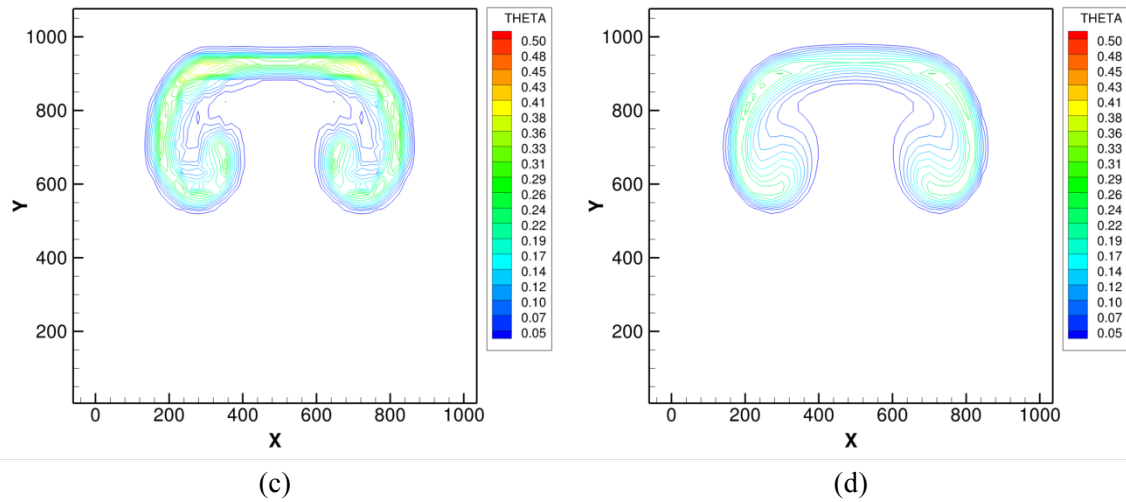
Figure 9. Potential temperature perturbation fields of the rising thermal bubble at $t = 700s$ using localized artificial viscosity and limiters with 20m resolution. (a) P^3 reconstruction on a 17×17 mesh with limiters; (b) P^{10} reconstruction on a 5×5 mesh with limiters; (c) P^3 reconstruction on a 17×17 mesh with localized artificial viscosity; (b) P^{10} reconstruction on a 5×5 mesh with localized artificial viscosity.

(a)   (b)

(c)   (d)
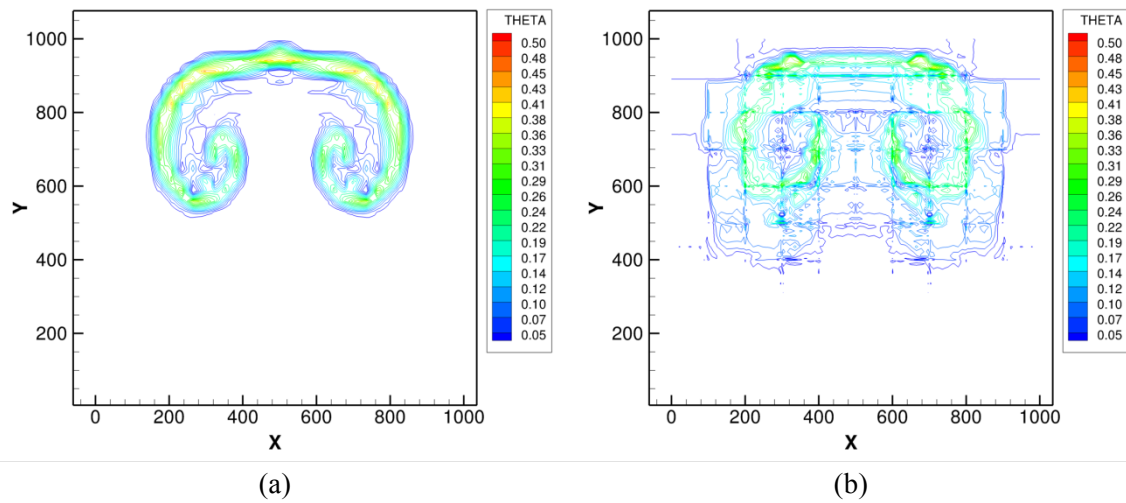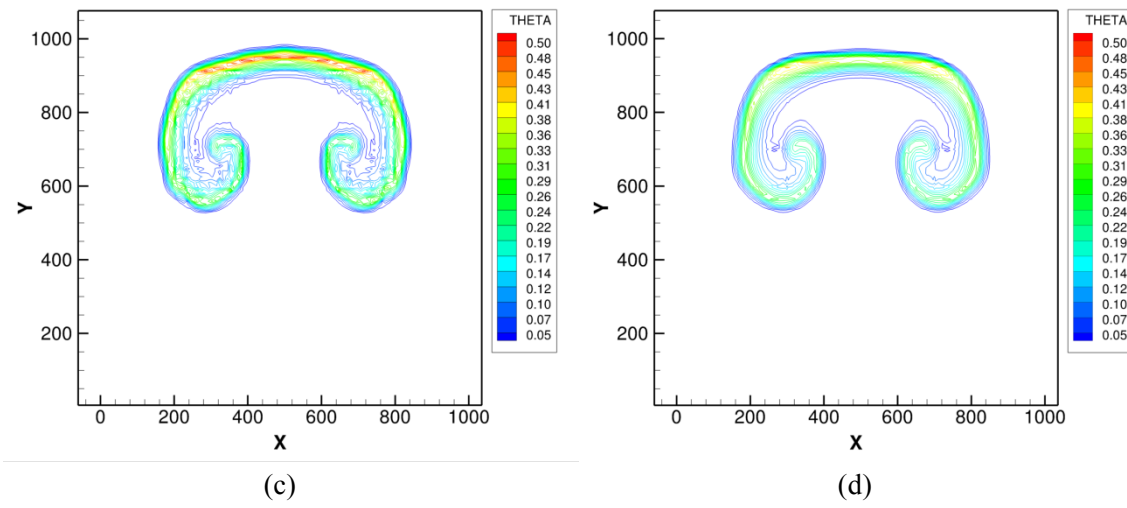
Figure 10. Potential temperature perturbation fields of the rising thermal bubble at $t = 700s$ using localized artificial viscosity and limiters with 10m resolution. (a) P^3 reconstruction on a $34{\times}34$ mesh with limiters; (b) P^{10} reconstruction on a $10{\times}10$ mesh with limiters; (c) P^3 reconstruction on a $34{\times}34$ mesh with localized artificial viscosity; (b) P^{10} reconstruction on a $10{\times}10$ mesh with localized artificial viscosity.

(a) $\mu = 0.1m^2/s$ (b) $\mu = 0.2m^2/s$

26

(c) $\mu = 0.3m^2/s$

(d) $\mu = 0.5m^2/s$

(e) $\mu = 1m^2/s$

(f) $\mu = 2m^2/s$
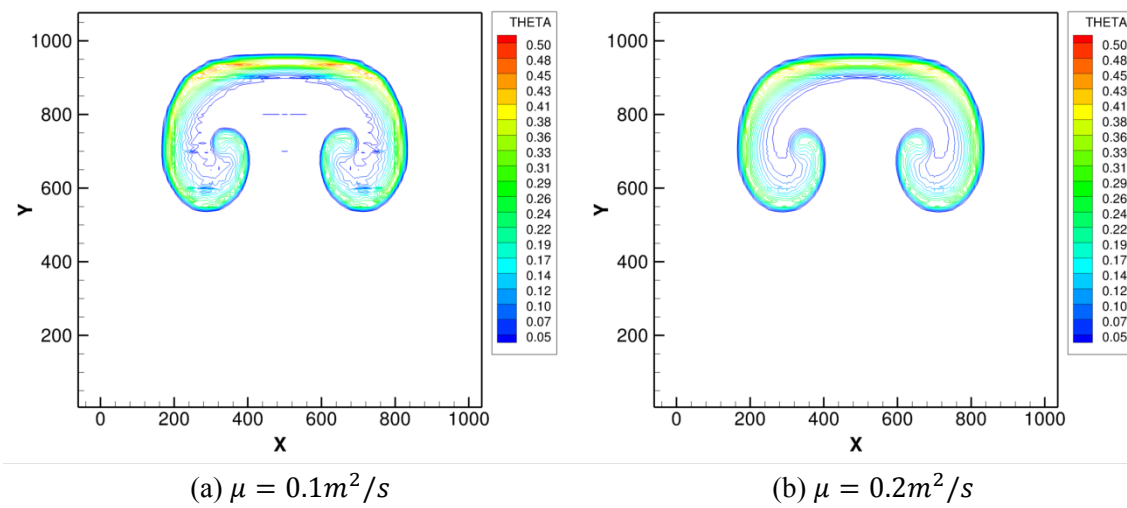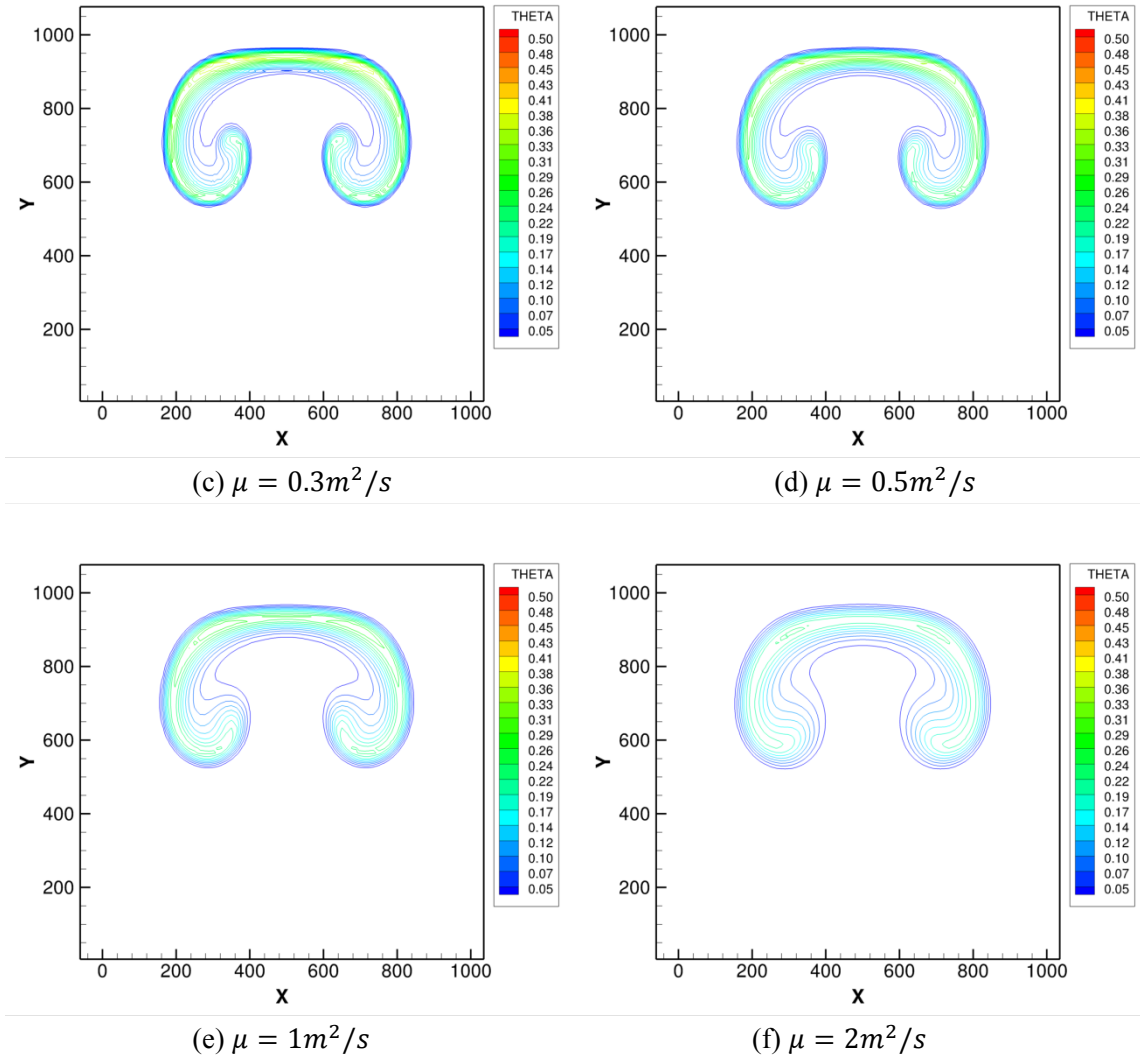
Figure 11. Potential temperature perturbation fields of the rising thermal bubble at $t = 700s$ for constant viscosity with different μ using P^{10} reconstruction on the $10{\times}10$ mesh.

	Max θ'	Min θ'
LAV	0.4409	$-6.196{\times}10^{-3}$
CV, $\mu = 0.1m^2/s$	0.4828	$-4.905{\times}10^{-2}$
CV, $\mu = 0.2m^2/s$	0.4404	$-2.115{\times}10^{-2}$
CV, $\mu = 0.3m^2/s$	0.4065	$-9.665{\times}10^{-3}$
CV, $\mu = 0.5m^2/s$	0.3611	$-1.919{\times}10^{-3}$
CV, $\mu = 1m^2/s$	0.3012	$-4.290{\times}10^{-5}$
CV, $\mu = 2m^2/s$	0.2431	$-1.655{\times}10^{-9}$

Table 2. The maximum and minimum potential temperature perturbations θ'_{max} and θ'_{min} of the rising thermal bubble at $t = 700s$ for localized artificial viscosity and constant viscosity with different μ using P^{10} reconstruction on a $10{\times}10$ mesh. LAV stands for localized artificial viscosity.
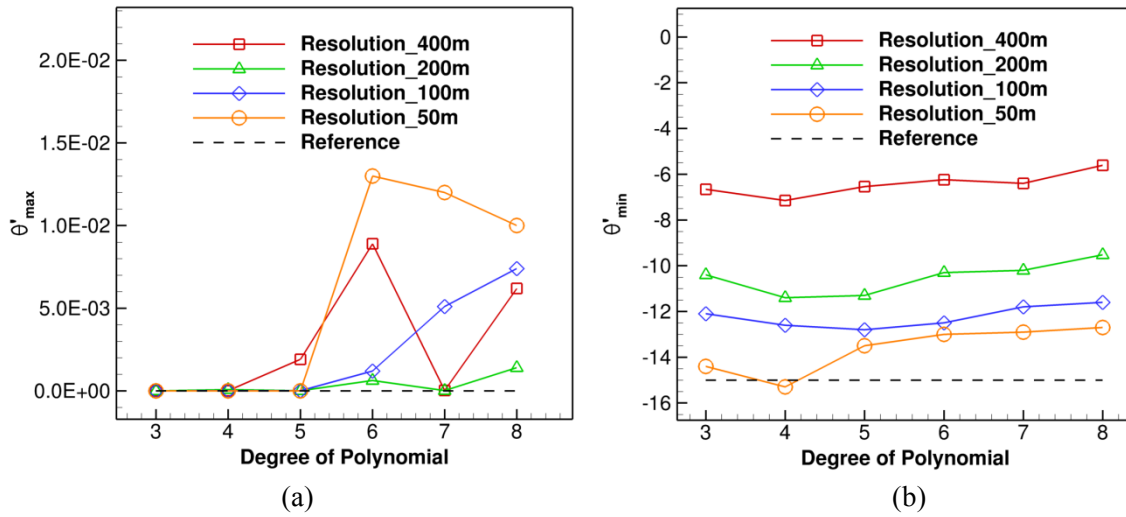
Figure 12. The maximum and minimum potential temperature perturbations θ'_{max} and θ'_{min} of the density current flow at $t = 900s$ with various flow field resolutions. (a) θ'_{max} vs. degree of polynomial; (b) θ'_{min} vs. degree of polynomial.
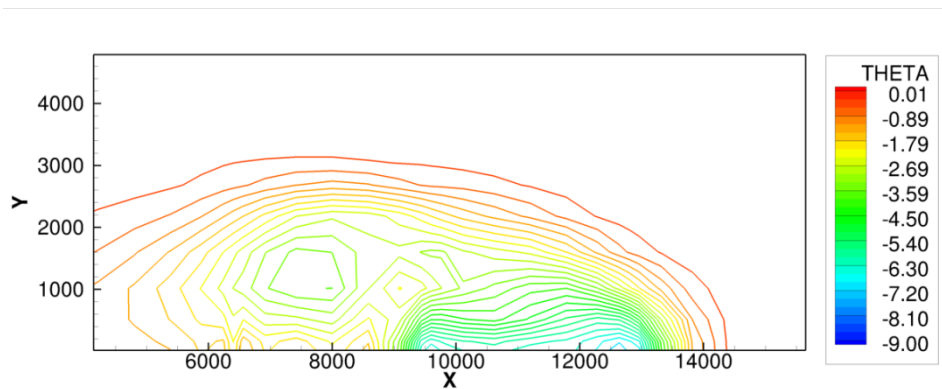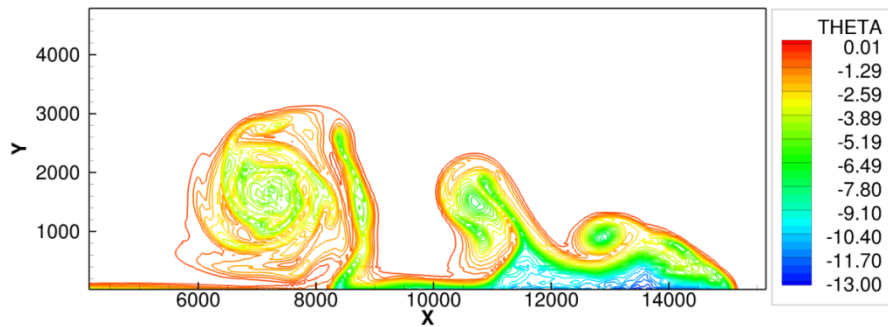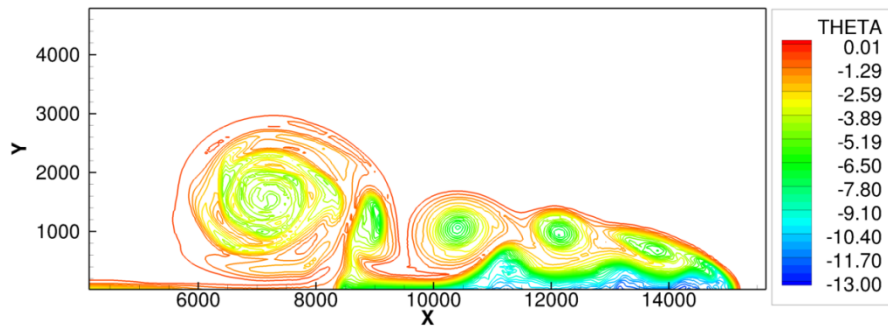

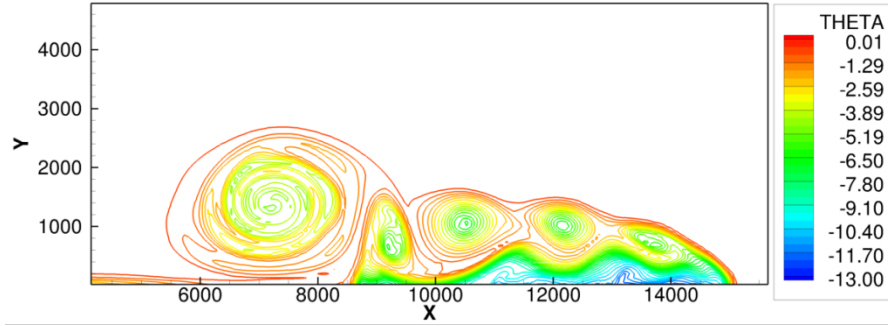(a) $\kappa = 0.25$
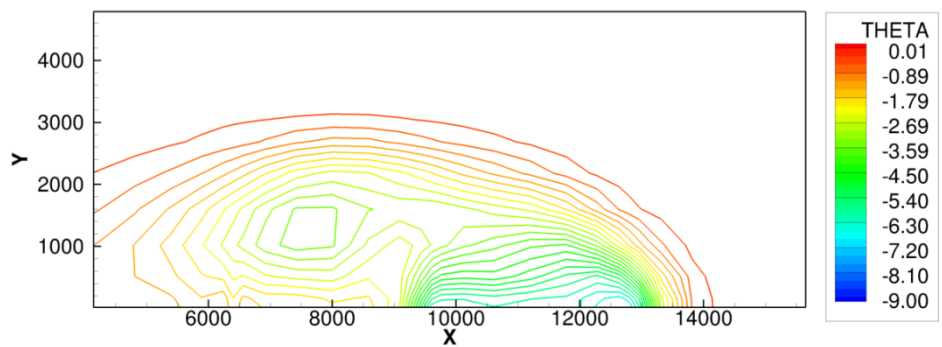
(b) $\kappa = 0.5$
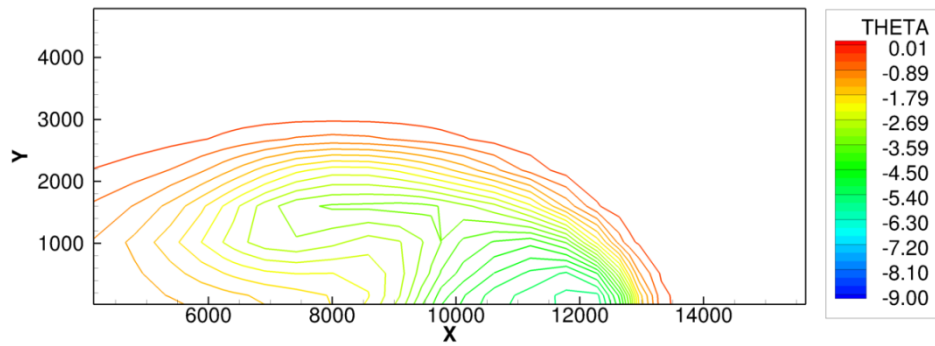
(c) $\kappa = 1$

Figure 13. Potential temperature perturbation fields of the density current at $t = 900s$ for different κ with P^8 reconstruction on the 8×2 mesh.
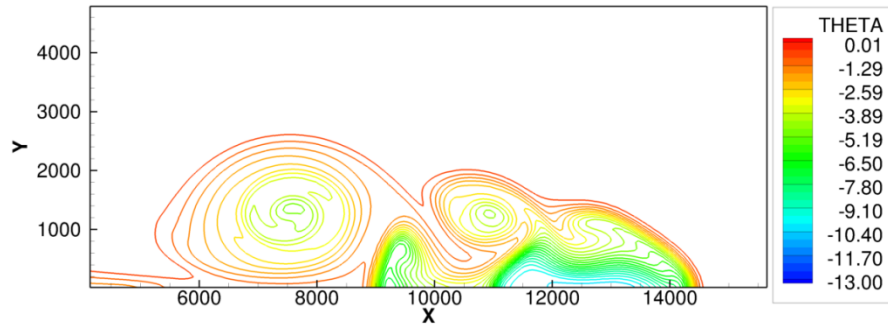

(a) $\kappa = 0.5$

(b) $\kappa = 1$

29

(c) $\kappa = 2$
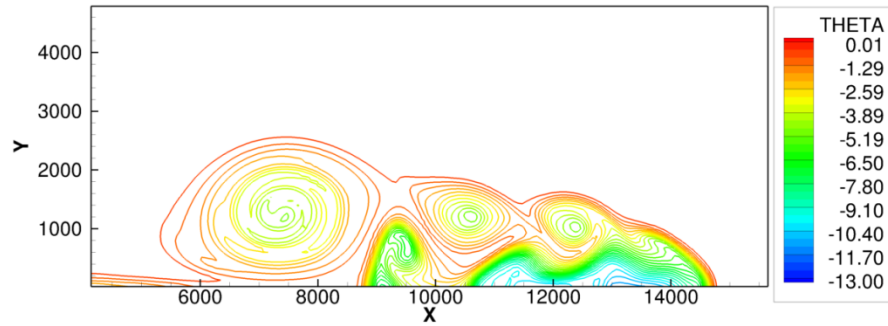
(d) $\kappa = 4$

(e) $\kappa = 6$

Figure 14. Potential temperature perturbation fields of the density current at $t = 900s$ for different κ with P^8 reconstruction on the 64×16 mesh.

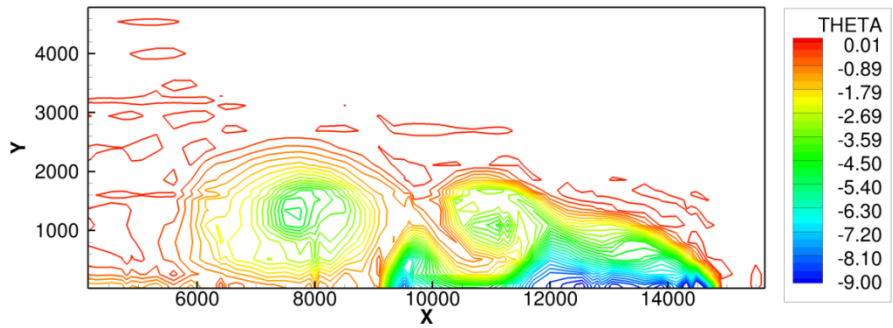| κ	Max θ'	Min θ'
0.5	1.425×10^{-2}	-13.59
1.0	7.743×10^{-3}	-14.60
2.0	4.007×10^{-4}	-12.17
4.0	4.740×10^{-8}	-11.03
6.0	2.457×10^{-8}	-10.33

Table 3. The maximum and minimum potential temperature perturbations θ'_{max} and θ'_{min} of the density current at $t = 900s$ for different κ with P^8 reconstruction on a 64×16 mesh.

30
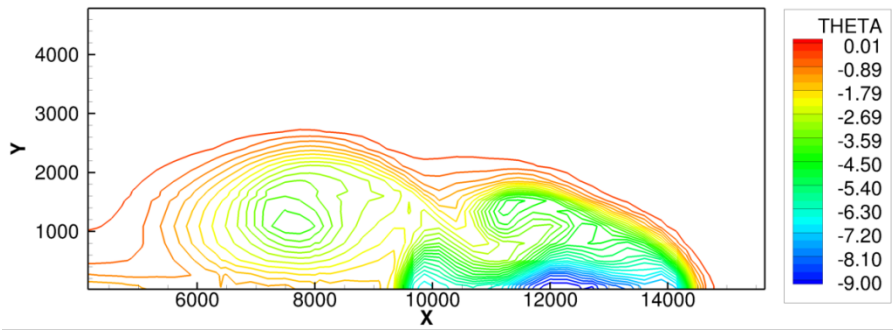
(a) LAV, $\kappa = 1$
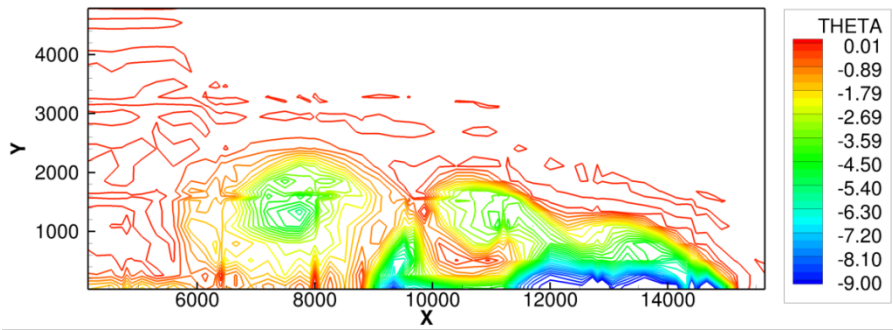
(b) $\mu = 50m^2/s$

(c) $\mu = 75m^2/s$

(d) $\mu = 100m^2/s$
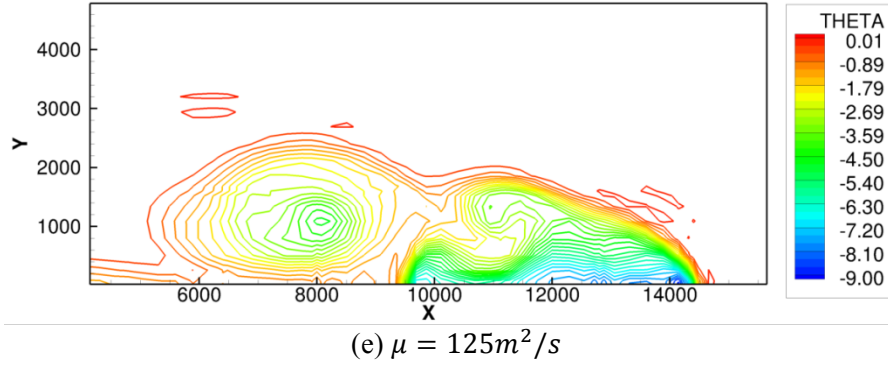
31
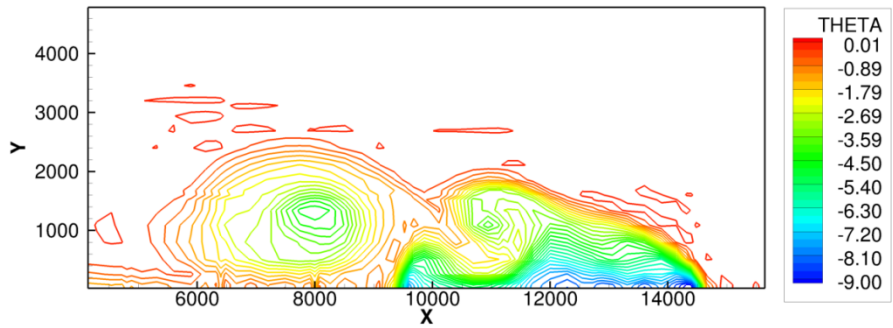
(e) $\mu = 125 m^2/s$

Figure 15. Potential temperature perturbation fields of the rising thermal bubble flow at $t = 700s$ for localized artificial viscosity and constant viscosity with different μ using P^8 reconstruction on the 16×4 mesh. LAV in (a) stands for localized artificial viscosity.

	Max θ'	Min θ'
LAV	4.753×10^{-4}	-9.548
CV, $\mu = 25 m^2/s$	Diverged	Diverged
CV, $\mu = 50 m^2/s$	8.161×10^{-1}	-12.39
CV, $\mu = 75 m^2/s$	1.981×10^{-1}	-10.85
CV, $\mu = 100 m^2/s$	1.369×10^{-1}	-9.387
CV, $\mu = 125 m^2/s$	9.243×10^{-2}	-8.835

Table 4. The maximum and minimum potential temperature perturbations θ'_{max} and θ'_{min} of the density current at $t = 900s$ for localized artificial viscosity and constant viscosity with different μ using P^8 reconstruction on a 16×4 mesh. LAV stands for localized artificial viscosity.